

## Article

# Terahertz Metamaterial Absorber Based on Ni–Mn–Sn Ferromagnetic Shape Memory Alloy Films

Rui Liu <sup>1</sup>, Xiaochuan Wang <sup>2</sup>, Jiachen Zhu <sup>3</sup>, Xiaohua Tian <sup>4</sup>, Wenbin Zhao <sup>2</sup>, Changlong Tan <sup>2,\*</sup> and Kun Zhang <sup>5,\*</sup> <sup>1</sup> School of Science, Harbin University of Science and Technology, Harbin 150080, China<sup>2</sup> School of Materials Science and Chemical Engineering, Harbin University of Science and Technology, Harbin 150080, China<sup>3</sup> School of Materials Science and Engineering, Harbin Institute of Technology, Harbin 150001, China<sup>4</sup> School of Electrical and Electronic Engineering, Harbin University of Science and Technology, Harbin 150080, China<sup>5</sup> Shenyang National Laboratory for Materials Science, Institute of Metal Research, Chinese Academy of Sciences, Shenyang 110016, China

\* Correspondence: changlongtan@hrbust.edu.cn (C.T.); kzhang@imr.ac.cn (K.Z.)

**Abstract:** Terahertz absorbers have been extensively investigated by researchers due to their applications in thermophotovoltaic energy conversion and sensors, but a key factor limiting their development is the lack of vital and versatile materials. Ferromagnetic shape memory alloys (FSMAs) offer a novel remedy for tunable metamaterials due to their brilliant recovery of deformation, remote control, and transient response. In this study, we propose a tunable absorber based on magnetic field tuning, consisting of Ni–Mn–Sn ferro-magnetic shape memory alloy films in fractal geometry and optically excited Si plates. Numerical analysis shows that the proposed absorber has an absorbance bandwidth of 1.129 THz above 90% between 1.950 THz and 3.079 THz. The absorber geometry can be regulated by an external magnetic field, allowing dynamic switching between broadband and narrowband absorption modes, the latter showing an ultra-narrow bandwidth and a high-quality factor  $Q$  of  $\sim 25.8$ . The proposed terahertz absorber has several advantages over current state-of-the-art bifunctional absorbers, including its ultra-thin structure of  $10.39 \mu\text{m}$  and an additional switching function. The absorption can be continuously tuned from 90% to 5% when the light-excited silicon plate is transferred from the insulator state to the metal state. This study presents a promising alternative strategy for developing actively regulated and versatile terahertz-integrated devices.

**Keywords:** metamaterials; shape memory alloy films; Ni–Mn–Sn alloy films; terahertz absorber; dynamic tuning



**Citation:** Liu, R.; Wang, X.; Zhu, J.; Tian, X.; Zhao, W.; Tan, C.; Zhang, K. Terahertz Metamaterial Absorber Based on Ni–Mn–Sn Ferromagnetic Shape Memory Alloy Films. *Metals* **2023**, *13*, 1162. <https://doi.org/10.3390/met13071162>

Academic Editor: Jiro Kitagawa

Received: 31 May 2023

Revised: 19 June 2023

Accepted: 20 June 2023

Published: 22 June 2023



**Copyright:** © 2023 by the authors. Licensee MDPI, Basel, Switzerland. This article is an open access article distributed under the terms and conditions of the Creative Commons Attribution (CC BY) license (<https://creativecommons.org/licenses/by/4.0/>).

## 1. Introduction

Based on the distinctive advantages of their photo energy and bandwidth, terahertz (THz) frequency waves have great potential for broad application in safety inspection, explosive detection, spectroscopy, medical imaging, wireless communications, etc. [1–5]. Tremendous research has been conducted in designing high-performance THz devices for the development of miniaturized components. Metamaterials (MMs) have recently emerged as perfect candidates for manipulating THz waves, attributable to their unique electromagnetic response mechanism [6–8]. Among them, THz metamaterial absorbers (TMMAs) are highly desired in a broad range of applications, including high-efficiency photodetectors, THz imaging, and stealth technology [9–11].

Research on TMMAs can be traced back to the concept of a perfect metamaterial absorber in the microwave range proposed by Landy et al. [12]. Since then, it has opened the door to developing TMMAs worldwide. Initially, conventional TMMAs consisted of a typical sandwich structure with a dielectric spacer, and these TMMAs showed narrowband absorption [13–15]. To enrich the functionalities, TMMAs with dual-, multi-,

and broadband absorption have been proposed and investigated in recent years [16–18]. Achieving broadband absorption of terahertz waves is still a challenge compared to visible and infrared light. In order to achieve broadband absorption, researchers have made many attempts, such as increasing the number of multiple distinct circular metallic patches, composite multi-layer stacking (vertical arrangement), introducing lumped elements, and the metal-dielectric nanocomposite systems [19–23], but these methods, although capable of achieving broadband absorption properties, also lead to a high cost of the proposed absorber, complex fabrication process, large size, and other drawbacks, which limit their practical applications. The above problem can be solved by using a fractal structure, which is a self-similar repetitive geometric structure in a fixed arrangement with a self-similar pattern leading to multiple resonant coupling, thus achieving broadband absorption [24–27]. More recently, the Cayley tree fractal meta-resonator supercells were proposed by Qasim Mehmood et al. [28]. They integrated different Cayley tree fractal resonators into one supercell based on the frequency shifting and multi-resonance bands of different fractal orders, which realizes broadband, polarization-insensitive ultrathin monolayer terahertz metamaterial absorbers. While broadband absorbers are mostly used in thermo-photovoltaics, narrowband perfect absorbers can be used in sensing, absorption filtering, and thermal radiation tailoring [29–32]. Most of the designs in the literature serve as either broadband or narrowband absorbers, and only a few studies achieve double functionality [33–41]. Combining both functionalities in the same device remains a significant challenge. Moreover, in conventional TMMAs, the resonance performance is determined by the structure parameters and material properties. Once fabricated, the THz absorber has non-adjustable absorption performance limiting its application. Although there have been studies on tunable materials with improved performance of tunable broadband terahertz metamaterial absorbers, the dilemma of multifunctional performance versus the complex multilayer structure of tunable TMMAs remains a problem. Therefore, designing thin and simple THz absorbers with tunable absorption performance remains highly desirable.

Different from the traditional metallic arrays of TMMAs, shape memory alloys (SMAs) exhibit distinctive functional characteristics, including superelastic behavior, shape memory effect, and work output with a high power/weight ratio [42,43]. Designing artificial metamaterial composed of shape memory alloys provides an active modulation by utilizing recoverable deformation and phase transformation in the subwavelength structures. This active adjustment has a bigger regulation region and reduces the complexity of the structure. In our previous works, Ni–Ti SMAs were innovatively introduced into the development of THz metamaterial devices [44,45]. Nevertheless, the slow martensitic transition response of Ni–Ti SMA is due to temperature-driven, magnetic-field-induced SMAs, which have attracted extensive research as a magnetoactuator material [46–48]. The controlling mode by a magnetic field is more flexible and quicker. Based on the FSMAs, it can be expected to achieve the dynamic tunability of terahertz metamaterial absorbers, which show the advantages of fast response and non-contact control.

In this paper, we propose a multifunctional, ultrathin, and high-performance TMMA by combining the horizontally aligned Cayley tree fractal meta-resonator supercells and the cross-shape resonator derived from Ni–Mn–Sn alloy films. The Cayley tree fractal meta-resonator supercells' host exhibits the desired broadband response, and the cross-shaped resonator exhibits the narrow-band response, while the aligned photoexcited Si layer modulates the resonance amplitude of the broadband absorber. Numerical results reveal that the absorption rate above 90% has a bandwidth of 1.129 THz from 1.950 THz to 3.079 THz. Notably, the function of broadband and narrowband absorption can be switched flexibly by applying a magnetic field. The narrowband mode shows an ultranarrow bandwidth and a high-quality factor  $Q$  of  $\sim 25.8$ . The terahertz absorber proposed in this work has many advantages over the present advanced absorbers, including a thin 10.39-micron structure. Moreover, the absorption rate can be continuously tuned from 90% to 5% when the photoexcited Si transits from the insulator state to the metal state. In

addition, the TMMA shows excellent performance in terms of polarization insensitivity and wide angle.

## 2. Structural Design and Method Simulation

The unit cell of the tunable TMMA that we designed is illustrated in Figure 1. It consists of Cayley tree metal resonators, a cross-shaped resonator, a photoexcited Si layer, a dielectric film, and a ground metal from top to bottom. The top layer of the unit cell consists of one, two, and three orders of fractal branches. To ensure polarization insensitivity, each branch is spaced apart with a  $120^\circ$  rotation angle, and the threefold rotational symmetry remains. The proposed structure uses the Cayley tree metal resonators to broaden the bandwidth. Simultaneously, the cross-shape resonator is added to the design for a narrowband. The metal of the Cayley tree metal resonators is Ni–Mn–Sn shape memory alloy films whose branches can be curved by applying an additional magnetic field, resulting in a switchable terahertz absorber from broadband to narrowband absorption. Ni–Mn–Sn is modeled as the lossy metal with a conductivity of  $3.3 \times 10^5$  S/m [49]. The continuous silicon has simulated a dielectric with constant permittivity  $\epsilon_{\text{Si}} = 11.9$  [50] and pump-power-dependent conductivity  $\sigma_{\text{Si}}$ . The dielectric permittivity of sapphire is 9.4 without a loss for the dielectric film [51]. The ground metal is selected as copper with a conductivity of  $5.96 \times 10^7$  S/m [52].

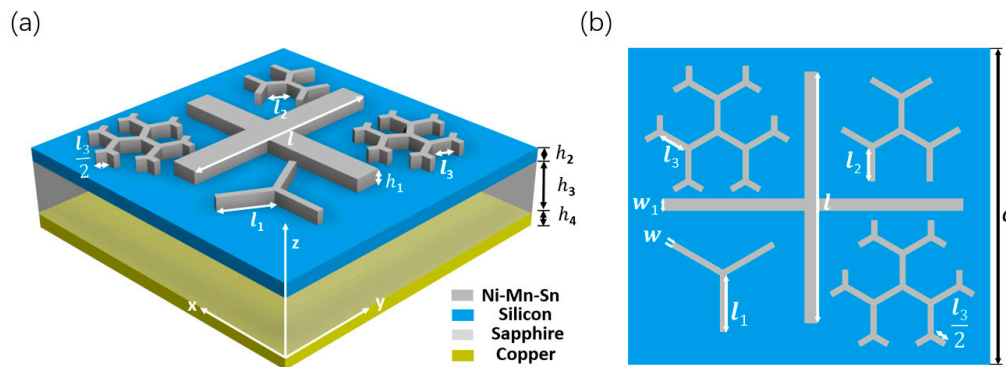


**Figure 1.** (a) 3D schematic of the designed switchable terahertz metamaterial unit cell. The unit cell is shown and includes the top metal (Ni–Mn–Sn) pattern over a bottom copper film separated by two dielectric spacers (Si and sapphire) with thicknesses  $h_1 = 0.2 \mu\text{m}$ ,  $h_2 = 0.1 \mu\text{m}$ ,  $h_3 = 10 \mu\text{m}$ , and  $h_4 = 0.1 \mu\text{m}$ , respectively. (b) The top view with detailed parameters. The arm length of the cross-shape is  $l = 40 \mu\text{m}$ , level 1 of the Cayley tree fractal is  $l_1 = 8 \mu\text{m}$ , level 2 is  $l_2 = 4.4 \mu\text{m}$ , and level 3 is  $l_3 = 5.8 \mu\text{m}$ , whereas the outer arm length of level 3 is  $l_3/2$ . The arm widths are  $w_1 = 2 \mu\text{m}$  and  $w = 1 \mu\text{m}$ , respectively. The period of the unit cell is  $a = 59 \mu\text{m}$ .

The principle of Ni–Mn–Sn resonant film deformation is shown in Figure 2. When an external magnetic field is applied, the magnetic Ni–Mn–Sn shape memory alloy undergoes an anti-martensitic phase transformation from antiferromagnetic martensite to ferromagnetic austenite, where the direction of the austenitic magnetic induction axis eventually coincides with the direction of the external magnetic field, resulting in a large magnetic strain. When the external magnetic field is released, the alloy undergoes a martensitic phase transformation and returns from austenite to martensite. This process provides cyclically reversible large-output strains.

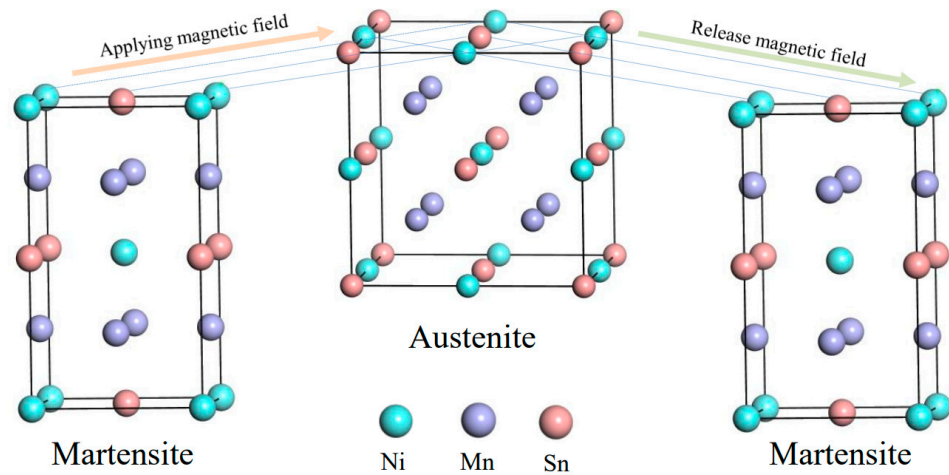


**Figure 2.** Schematic diagram of magnetic field induced Ni–Mn–Sn martensite phase transformation.

The materials present in nature are composed of atoms, and the electromagnetic response is determined with the dielectric constant and the magnetic permeability. Its response frequency and dielectric constant follow the Drude–Lorentz relationship:

$$\varepsilon_{eff}(\omega) = 1 - \frac{\omega_p^2}{\omega^2 - \omega_0^2 - i\gamma\omega} \quad (1)$$

The plasma frequency is determined with the following equation:

$$\omega_p = \frac{4\pi ne^2}{m^*} \quad (2)$$

where  $\omega_0$  is the resonant frequency,  $n$  is the carrier density,  $e$  is the charge of the electron,  $\gamma$  is the damping coefficient, and  $m^*$  is the carrier effective mass.

The absorber proposed in this paper is based on this principle, the designed sub-wavelength structure is atom-like, and the periodic macroscopic repetitive unit structure constitutes the whole metamaterial; therefore, its electromagnetic response is related to the subwavelength unit structure [49].

In this paper, Ni–Mn–Sn films are used as resonant structures because, in addition to their unique shape memory effect, they have a high virtual refractive index (R.I.) that can be sufficient to provide excellent absorption. The refractive index  $n$ , effective permittivity  $\varepsilon_{eff}$ , and magnetic permeability  $\mu_{eff}$  of the metamaterial satisfy the following relationship:

$$n = \sqrt{\varepsilon_{eff}\mu_{eff}} \quad (3)$$

The martensitic phase transformation of Ni–Mn–Sn SMAs is accompanied by a change in shape as well as a change in material properties, both of which are actively modulated, affecting the electromagnetic response in terms of terahertz wave transmission characteristics and reflection properties. Among them, the dielectric constant is the direct evidence to characterize the change in material properties. Therefore, the mechanism of dynamic modulation of the electromagnetic response of metamaterials by shape memory alloys can be fully explained by using the variation of the dielectric constant. According to the Drude model, the permittivity in the terahertz band can be characterized with the following equation:

$$\varepsilon_m \approx -\sigma_{dc}/(\varepsilon_0\Gamma) + i\sigma_{dc}/(\varepsilon_0\omega) \quad (4)$$

where  $\sigma_{dc}$  is the direct current conductivity,  $\Gamma$  is the damping rate, and  $\varepsilon_0$  is the vacuum dielectric. The outcome of THz–TDS is excellent, consistent with the simplified Drude model. In summary, both the real and imaginary parts of the permittivity contain direct

current conductivity, so that the change in permittivity can be described by the change in conductivity. Accordingly, it is possible to directly characterize the reform in material properties throughout the martensitic phase transformation of SMAs in terms of electrical conductivity. In this simulation, we chose the Ni–Mn–Sn SMAs' conductivity before and after the phase change within the bounds of  $3.3 \times 10^5$  S/m to  $7.6 \times 10^5$  S/m.

Intending to analyze the performance of the designed absorber, simulations were performed using CST MICROWAVE STUDIO® (CST Computer Simulation Technology GmbH, Darmstadt, Germany). The unit cell condition should be defined at the  $x$  direction and  $y$  direction for the boundary condition, and the open (add space) was defined at the  $z$  direction for the boundary condition [53]. We defined the transverse electric (TE) polarization mode as the electric field parallel along the  $y$ -axis and the magnetic field parallel along the  $x$ -axis when the THz wave is normal incidence to the introduced absorber. Transverse magnetic (TM) polarization mode is the opposite. The unit cell's geometrical parameters of the absorber were optimized at  $h_1 = 0.1$   $\mu\text{m}$ ,  $h_2 = 0.1$   $\mu\text{m}$ ,  $h_3 = 10$   $\mu\text{m}$ ,  $h_4 = 0.1$   $\mu\text{m}$ ,  $l_1 = 8$   $\mu\text{m}$ ,  $l_2 = 4.4$   $\mu\text{m}$ ,  $l_3 = 5.8$   $\mu\text{m}$ ,  $w = 1$   $\mu\text{m}$ , and  $w_1 = 2$   $\mu\text{m}$ . However, in level 3 of the Caley tree fractal meta-resonator supercells, the outermost arm lengths were set to  $l_3/2 = 2.9$  to prevent overlapping of neighboring structures. The metallic copper substrate leads to a transmittance of 0 (i.e.,  $S_{21} = 0$ ). The absorbance was calculated as  $A(\omega) = 1 - R(\omega) - T(\omega) = 1 - |S_{11}|^2 - |S_{21}|^2 = 1 - |S_{11}|^2$ .

In addition, the method of sample fabrication is important to the terahertz components. Recently, MEMS processing technology, such as the etching of silicon substrates, has made great progress [54] with thin-film deposition prior to gluing or by choosing a substrate with a thin film, such as silicon. Sapphire (epitaxial silicon on sapphire) and the desired structure are obtained by etching after hardening. During the etching process, the photoresist acts as protection, and the resulting structure has the same shape as the photoresist to ensure that the Caley tree structure in the proposed metamaterial is fixed to the silicon surface and remains stable without falling off. It is necessary to deposit a metal copper thin film on the Si layer with a method similar to the Refs. [55,56] thin-film structure, and then deposit the SMA layer on the copper thin film.

### 3. Results and Discussion

#### 3.1. Broadband THz Absorber

The simulated absorption spectra of the Ni–Mn–Sn-based absorber are shown in Figure 3. Figure 3a–d shows the simulated absorption spectra of the first, second, and third iteration of the proposed Caley tree resonating structures and the cross structure. For each structure, they cannot achieve broadband absorption independently. However, broadband absorption can be achieved by combing these four structures into one supercell, as shown in Figure 3e. It is observed that the absorption magnitude of the introduced metamaterial is more than 90% in the frequency range from 1.950 THz to 3.079 THz, suggesting that the proposed absorber has an excellent absorption performance. It is worth mentioning that the peak absorption magnitude is observed at multiple frequencies, i.e., 2.101, 2.524, and 2.692 to 3.019 THz. The near-unity absorption broadband spectrum caused by the mechanism of multiple resonance peaks originates from the different orders of the Caley tree fractal resonators [27]. Therefore, self-similar fractals are proposed as an ideal candidate for ultra-broadband absorbing devices due to the multiscale geometric features involved, which provide a degree of freedom for varying the resonance frequency.

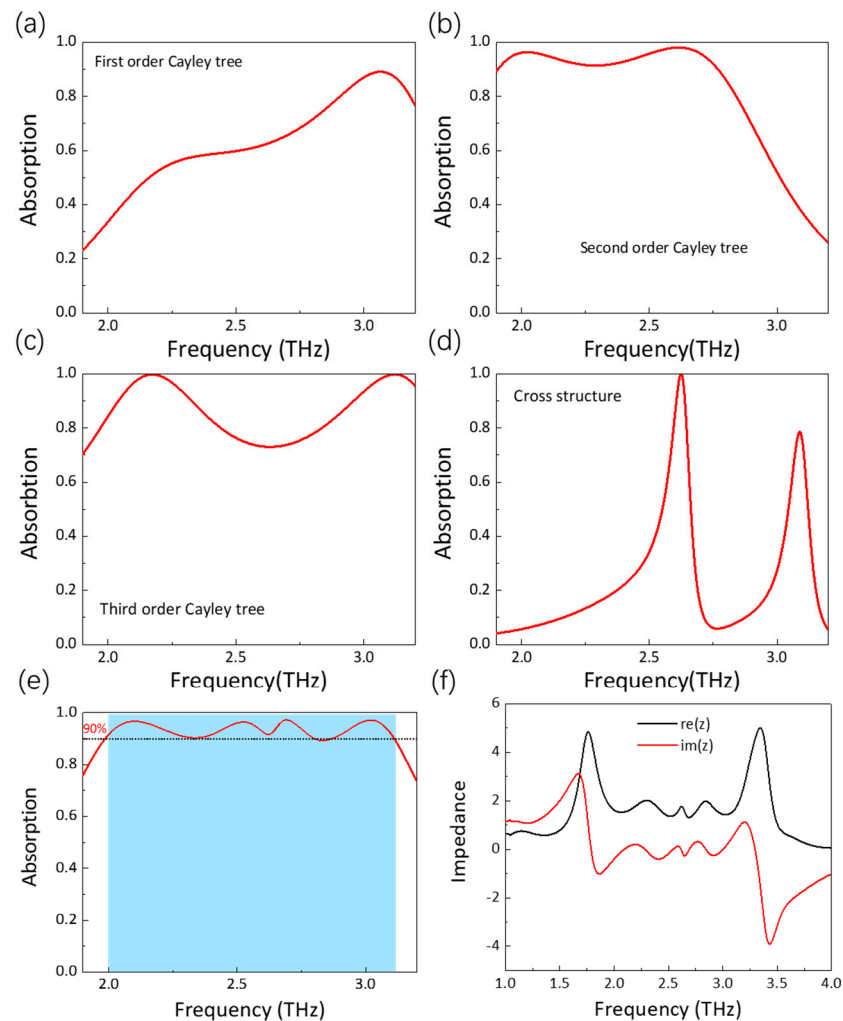


**Figure 3.** Absorption spectrum. (a) Absorption of first–order Cayley tree, (b) absorption of second–order Cayley tree, (c) absorption of third–order Cayley tree, (d) absorption of cross structure, (e) absorption spectrum of broadband terahertz metamaterial cell design. The 90% absorptivity and bandwidth are indicated by the short dotted line and shallow blue area, respectively. (f) Normalized effective impedance spectrum of the broadband terahertz metamaterial.

In addition, the relative bandwidth of the introduced absorber is also calculated through  $f_c = 2(f_H - f_L)/(f_H + f_L)$ , where  $f_H$  is the upper frequency,  $f_L$  is the lower frequency, and the relative bandwidth  $f_c$  is 45%. In order to reveal the working mechanism of the introduced single-layer Ni–Mn–Sn broadband absorber, we retrieved the corresponding effective impedance using the S-parameter extraction method [57,58]. The effective impedance can provide insight into understanding the optical response of the proposed metamaterial absorber. The relative impedance can be given by

$$Z_{eff}(\omega) = \pm \sqrt{\frac{(1 + S_{11})^2 - S_{21}^2}{(1 - S_{11})^2 - S_{21}^2}}, \quad (5)$$

where  $S_{11}$  and  $S_{21}$  are the complex reflection and transmission coefficients, respectively. Figure 3f shows the real and imaginary sections of the effectual impedance for the introduced metamaterial broadband absorber. The most significant finding to emerge from the following graph is that the real section is a short distance from 1, and the imaginary section is in the neighborhood of 0 from 1.950 THz to 3.079 THz. This phenomenon is consistent with the effectual impedances of the introduced metamaterial absorber matching

better to the impedance of the free space, resulting in high absorption intensity. The large bandwidths are thought to be owed to the coupling of the adjacent resonances. Gottheim et al. proposed a detailed qualitative analysis to describe the mode degeneracies and origin of distinct absorption peaks in Cayley tree fractal geometry metamaterials [27]. In conclusion, the strong resonance frequency is mainly due to the first, second, and third fractal orders or the interaction between two levels.

### 3.2. Switchability between Broadband and Narrowband Absorption under the Magnetic Field

A significant bandwidth decline in the absorber can be driven by the structure change in the metamaterial Ni–Mn–Sn while applying an extraneous magnetic field. To understand the structural conversion of metamaterial in the shape of a Cayley tree fractal based on Ni–Mn–Sn, we characterized the absorption at different curved angles ( $\theta$ ) of the Cayley tree fractal resonators as schematically shown in Figure 4a. The simulated absorption spectrum was taken for the initial pristine structure of the absorber introduced, and the bendable part of the Cayley tree fractal resonators was curved to  $20^\circ$ ,  $30^\circ$ ,  $40^\circ$ , and  $50^\circ$  (Figure 4b). The absorption patterns of the introduced device showed absorption peaks associated with the Cayley tree fractal resonators. The narrowband forms at the interface between the Ni–Mn–Sn in a cross shape and the copper ground plane during the Ni–Mn–Sn Cayley tree fractal metamaterials' deformation process. After the Ni–Mn–Sn Cayley tree fractal metamaterials were curved to  $50^\circ$ , the broadband peaks disappeared. Only the narrow peak was still visible, and its absorption intensity was still maintained above 90%. This is consistent with the disappearance of the initial Ni–Mn–Sn Cayley tree fractal metamaterial in a plane and the formation of Ni–Mn–Sn cross-shape metamaterial independent. It should be mentioned that, although the Cayley tree part and the cross-shape part are both made of Ni–Mn–Sn FSMAs, their magnetic-induced martensitic transformation behavior can be controlled independently due to the slight difference in their alloy compositions and martensitic transformation temperatures [59,60]. When the Ni–Mn–Sn SMAS film in the proposed absorber is in the austenitic state, the absorber has the function of a broadband absorber, which is indispensable in thermophotovoltaic, photodetection, calorimetric, and mechanical resonance operations [25]. As the applied magnetic field increases, the martensitic phase transformation is gradually complete, and the Ni–Mn–Sn FSMAs undergo a shape change so that the absorber gradually changes from a broadband absorber to a narrowband absorber. Narrowband absorbers are widely used in food quality monitoring, disease diagnosis, biosensing, and other fields [40].

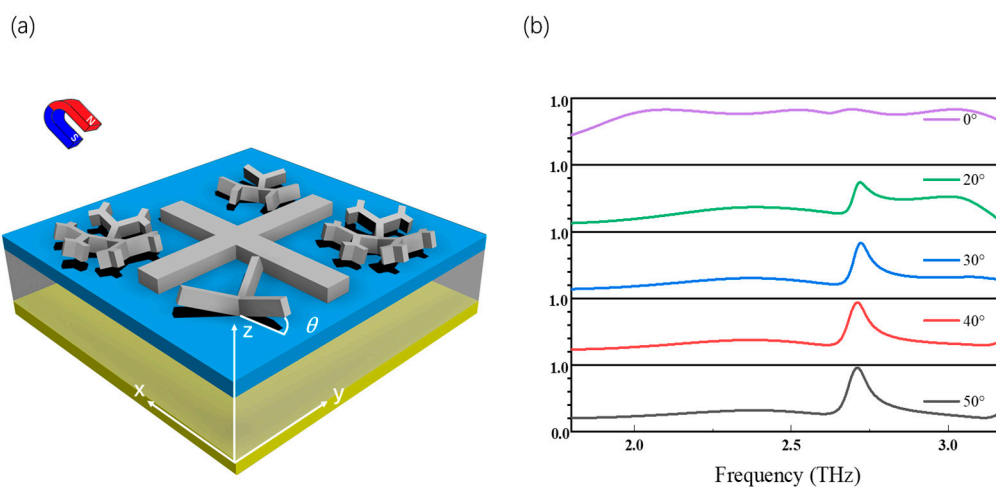


**Figure 4.** (a) Schematic drawing of Cayley tree fractal-shape metamaterials with different curved angles  $\theta$  under an external magnetic field. (b) The calculated absorptances with different curved angles  $\theta$  of Ni–Mn–Sn metamaterials in the shape of a Cayley tree fractal.

### 3.3. Multifunction under the Optical Pump

Further research will explore the influence of electromagnetic corresponding under the pump-power optical control on silicon film [61], as schematically shown in Figure 5a. When light shines on silicon, the light intensity increases, and the light carrier in extremely resistive silicon increases, leading to an increase in its electrical conductivity. A dynamic tunable intensity of absorption can be observed by changing the conductivity of photoexcited Si, as indicated in Figure 5b. The simulated absorption spectrum shows switching regimes from 1.950 THz to 3.079 THz frequencies with reasonably high contrast. From 1.950 THz to 3.079 THz, the metamaterial switches from a high-absorption state at small conductivity of Si to a low-absorption state at high conductivity of Si as the photoexcited Si changes its state from an insulating state to a metallic state. We observe that the absorption of the metamaterial structure decreases from 95% to 5% when the conductivity of Si increases from 1 S/m to  $1 \times 10^6$  S/m [62,63]. Based on the Drude model, the photoexcited carrier mass results in an increase in the imaginary section of the dielectric constant, which leads to a bigger decrease when terahertz waves after the silicon wafer [64]. This phenomenon can be attributed to photoexcited Si due to the generated free carriers screening the confined resonant fields, which cannot store electromagnetic energy in the introduced device [65].

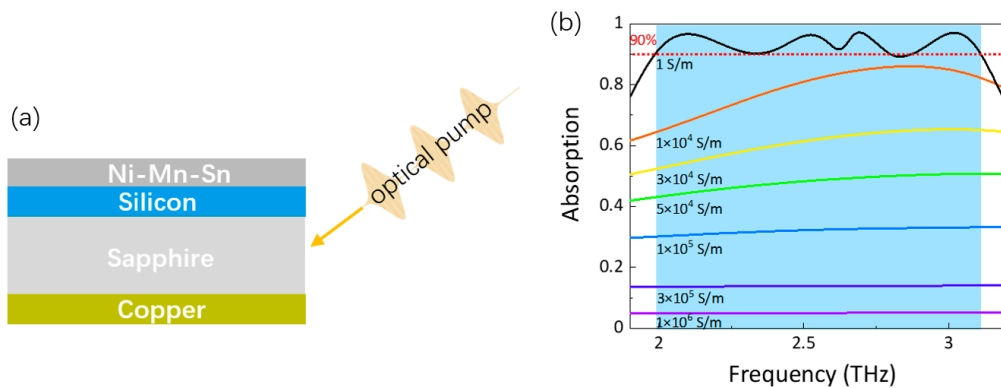


**Figure 5.** (a) Schematic of the terahertz metamaterial absorber side view under optical stimulus focus on the Si film. (b) The calculated absorptances with different conductivities of photoexcited Si. At a given resonance frequency, when 400 nm is incident on ion-irradiated Si, the photoconductivity of Si ( $\sigma$ ) increases, thereby leading to the modulation of resonance strength.

As a result, the switching intensity of 90% is obtained in the switching range of 1.129 THz, and the corresponding switching contrast (SC), defined as  $SC = (A_{max} - A_{min})/A_{min}$ , is calculated to be at least 1700% and can be improved by further increasing the conductivity of silicon, which is above six times higher than the previously reported results [66].

As the simulation results show, by using an applied magnetic field to drive the deformation of the shape memory alloy, we can achieve the conversion between wide/narrow absorbers and the function of absorber switching. In order to describe more clearly the advantages of this work, we compared it with some recently proposed tunable absorbers, as shown in Table 1. In addition, switching the total quality factor  $Q$  of the narrow-band absorber function with a maximum value  $Q$  of approximately 25.8 has potential applications in the sensing field. It is worth mentioning that the deformation of Ni–Mn–Sn SMAs by magnetic field modulation greatly reduces the complexity of the terahertz metamaterial design and facilitates device integration.

**Table 1.** Comparison of absorption performance between different absorbers.

References	Function	Working Bandwidth	Absorptance	Tunable Range	Material	Regulating Method
[30]	Switching	1.85–4.3 THz	>90%	4–100%	VO <sub>2</sub>	Temperature
[31]	Switching	4.29–5.52 THz	>90%	4–100%	VO <sub>2</sub>	Electric field
[32]	Switching	1–2.03 THz	>90%	0–99%	Graphene, VO <sub>2</sub>	Temperature, Electric field
[34]	Wide-narrow	3.57–8.45 THz	>50%	—	VO <sub>2</sub>	Temperature
[36]	Switching	1.2–2.67 THz	>90%	0–95%	MoS <sub>2</sub>	Temperature
[16]	Wide-band	500–3000 nm	>90%	—	—	—
[20]	Dual-band	200–1000 nm	>90%	—	Au/Cr/3 layers of grapheme/TMDs pair	—
This Work	Wide-narrow/Switching	1.950–3.08 THz	>90%	5–95%	Ni–Mn–Sn	Magnetic Fields

### 3.4. Incident Angle Sensitivity Characteristics

By rotating the direction incident to the terahertz wave placed in front of the terahertz metamaterial absorber, we further investigate and explore the incident angle sensitivity particularities of the broadband absorber. When the direction of the incident terahertz is perpendicular to the broadband absorber, the absorption intensities located at 1.950 THz to 3.079 THz are the maximum values, and the direction of the incident terahertz wave at this moment is set as the starting point (recorded as 0°). As shown in Figure 6a, when rotating the direction of the incident terahertz wave to 40°, the multi-resonance modes are both interaction modes, resulting in broadband and outstanding absorption. Analyzing the normalized curves of the absorption intensities of the TM mode shown in Figure 6b, the curves are approximately the same from 0° to 40°, which illustrates that the multi-resonance modes have the same interaction state. Therefore, it can be concluded that a stable broad-wavelength absorber can also be obtained even if the incident angle of the modes is 40°, which can be used to generate broadband absorption through the design introduced.

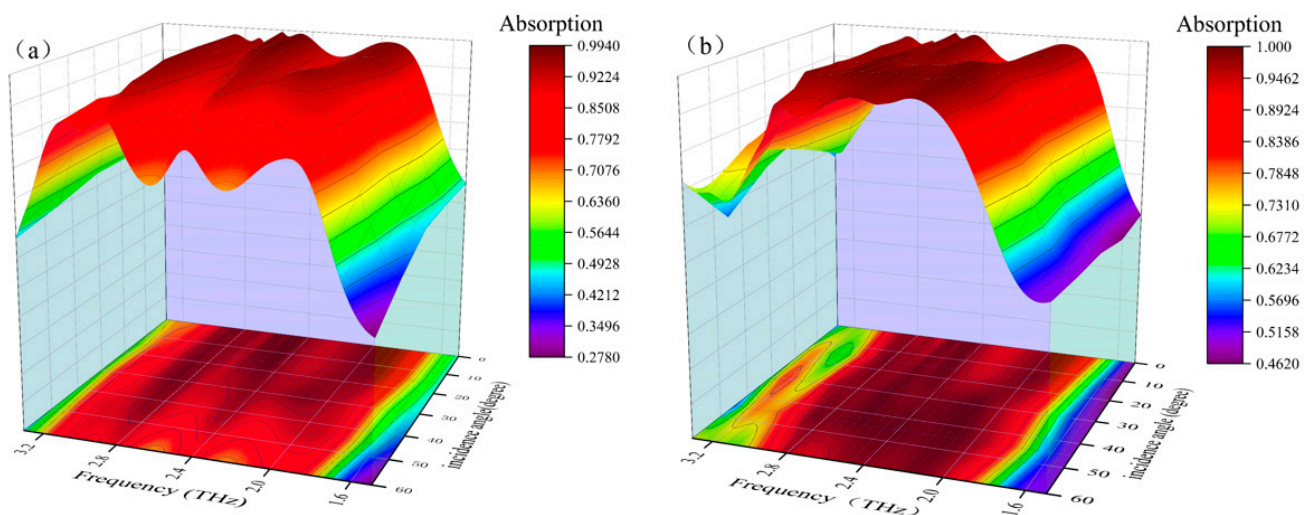


**Figure 6.** Numerically simulated incident angle dependent of the broadband terahertz metamaterial absorber: (a) TE mode and (b) TM mode.

### 3.5. Mechanism of Wide/Narrow Band Absorption Conversion under Magnetic Field

To comprehend the mechanism of forming narrowband absorption, the distributions of surface current and electric field are simulated and analyzed at the specific resonance frequency, as shown in Figure 7. Color maps and arrows denote the strength of the field and current, respectively. The electric field accumulates mainly in both ends of the vertical branches of the Ni–Mn–Sn cross shape when the incident wave is applied as a TE-polarization wave; for TM-polarized waves, the electric field concentrates mainly

around the edges of the horizontal branches. The electric field distributions demonstrate that the incident terahertz wave excites typical electrical dipole resonances at the topside surface of the Ni–Mn–Sn cross patch along the  $y$  and  $x$  directions, respectively, for different polarization terahertz wave incidents (see Figure 7a,d).

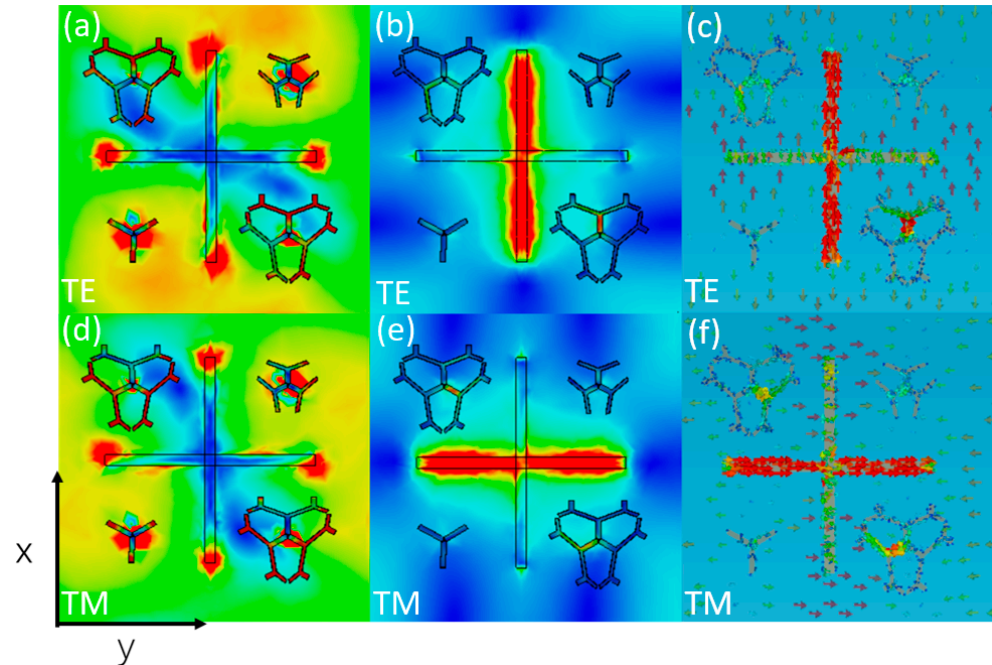


**Figure 7.** Distributions of (a,d) electric, (b,e) magnetic fields, and (c,f) surface currents at the resonant frequency of 2.71 THz for TE and TM-polarized THz wave in the inward propagation.

The contour map of the magnetic field distribution in the introduced absorber in the  $x$ - $y$  plane is shown in Figure 7b,e. As revealed, the magnetic fields of the absorption band are all distributed over the cross shape of the narrowband superabsorber, which confirms the localized resonance characteristics of the absorption bands. However, the magnetic field distribution positions of the TE and TM polarizations are different. For TE-polarized waves, the magnetic field is mainly concentrated at the upright strip. Similar to the TM polarization wave, the magnetic field is mostly gathered at the horizontal strip. The arrows in Figure 7c,f represent the intensity and flowing directions of the surface current distributions on the top cross resonator and bottom ground plane. The surface current distribution of the TE polarization waves on the Ni–Mn–Sn SMA resonant films is principally around the  $x$ -axis direction, while the surface current on the metallic copper substrates is parallel to its inverse. Consequently, a magnetic polariton is considered [67], which can result in a large magnetic resonance and a deep, resonant dip in the reflection spectrum [68]. Meanwhile, for the TM-polarized waves, the anti-parallel surface currents give rise to the front resonator and back substrate along the horizontal direction, forming an equivalent current loop. The existence of excited electromagnetic resonance confines the incident terahertz waves in the absorber. It utilizes the ohmic loss in the metal, and the dielectric loss in the dielectric layer dissipates the incident terahertz waves in the absorber. Eventually, the perfect narrowband absorber was demonstrated with absorption, which is approximately 100%.

### 3.6. The Feasibility of Experimental Demonstration

Based on the simulation results above, we have systematically studied and demonstrated the possibility of our design. Here, the feasibility of the experimental demonstration is discussed and analyzed. Despite the fact that follow-up experiments are not executed in the existing research, a significant amount of associated works have proved that the

fabrication of our proposed absorber can be realized with inexpensive cost and excellent precision. First, as an advanced actuator and sensor, shape memory alloys are used commercially in many fields, such as the magnetic actuators in automotive applications [69], the micro-actuators or artificial muscles in robotic applications [70], Boeing's variable geometry chevron in aerospace application [71], and so on. Moreover, with the development of SMA nano/micro-scale properties [72], shape memory alloy films with ultra-small sizes have been fabricated and used in micro-electro-mechanical systems (MEMS) [73]. The application of magnetic field-driven SMAs in terahertz devices has been successfully demonstrated experimentally [74]. In our work, the design of a terahertz absorber dependent on Ni–Mn–Sn FSMA films is simply attributable to the distinctive functional behaviors, for instance superelasticity and shape memory effects, and the magnetic field is easy and fast to apply. It is reasonable to expect that our proposed terahertz absorber will be successful in practical applications. However, Ni–Mn–Sn suffers from weak deformation recovery and large losses. In addition, the applied magnetic field to drive the magnetic Ni–Mn–Sn phase transition is large. This limits their practical application. These problems can be solved by adjusting the composition of the shape memory alloy and improving the fabrication process in our subsequent work.

#### 4. Conclusions

In summary, we present a versatile, ultrathin, superior performance terahertz absorber with Ni–Mn–Sn FSMAs. The absorber enables the interconversion of broadband absorption and narrowband absorption. Numerical results show that the absorption rate is maintained above 90% in the 1.129 THz bandwidth from 1.950 THz to 3.079 THz. The magnetic field can modulate the absorber to switch between broadband and narrowband absorbers with the narrowband mode exhibiting an ultra-narrow bandwidth and a high-quality factor  $Q$  of  $\sim 25.8$ . In addition, the device can dynamically adjust the absorption rate from 90% to 5%. Notably, the absorber is insensitive to incidence angle, which allows for a wider range of applications. The terahertz absorber proposed in this work has many advantages over the present advanced absorbers, including the advantages of ultra-wide operating frequency, excellent absorption efficiency, and transient response. This work supports new ideas for the development of dynamically adjusted multifunctional terahertz functional components, and the proposed devices have potential applications in fields such as thermophotovoltaic energy conversion and sensors. The weak recovery of Ni–Mn–Sn deformation and the large driving magnetic field limit the practical application of the proposed absorber. However, these problems can be solved by tuning the composition of shape memory alloys and improving the fabrication process in our subsequent work.

**Author Contributions:** Conceptualization, K.Z. and C.T.; investigation, methodology, R.L. and X.W.; writing original draft preparation, R.L. and X.W.; writing—review and editing, K.Z. and C.T.; formal analysis, J.Z., X.T. and W.Z.; supervision, C.T. and K.Z.; resources and funding acquisition, J.Z., X.T., C.T. and K.Z. All authors have read and agreed to the published version of the manuscript.

**Funding:** This research is funded by the Heilongjiang Provincial Natural Science Foundation of China (Grant No. YQ2022112); the National Natural Science Foundation of China (Grant Nos. 51871083, 51971085, 52001101, 52271172).

**Data Availability Statement:** The data presented in this study are available upon request from the corresponding author.

**Conflicts of Interest:** The authors declare that they have no known competing financial interests or personal relationships that could have appeared to influence the work reported in this paper.

#### References

1. Lu, M.; Shen, J.; Li, N.; Zhang, Y.; Zhang, C.; Liang, L.; Xu, X. Detection and identification of illicit drugs using terahertz imaging. *J. Appl. Phys.* **2006**, *100*, 103104. [[CrossRef](#)]
2. Davies, A.G.; Burnett, A.D.; Fan, W.; Linfield, E.H.; Cunningham, J.E. Terahertz spectroscopy of explosives and drugs. *Mater. Today* **2008**, *11*, 18–26. [[CrossRef](#)]

3. Beard, M.C.; Turner, G.M.; Schmuttenmaer, C.A. Terahertz spectroscopy. *J. Phys. Chem. B* **2002**, *106*, 7146–7159. [[CrossRef](#)]
4. Taylor, Z.D.; Singh, R.S.; Bennett, D.B.; Tewari, P.; Kealey, C.P.; Bajwa, N.; Culjat, M.; Stojadinovic, A.; Lee, H.; Hubschman, J.-P.; et al. THz medical imaging: In vivo hydration sensing. *IEEE Trans. Terahertz Sci. Technol.* **2011**, *1*, 201–219. [[CrossRef](#)] [[PubMed](#)]
5. Federici, J.; Moeller, L. Review of terahertz and subterahertz wireless communications. *J. Appl. Phys.* **2010**, *107*, 6–323. [[CrossRef](#)]
6. Chen, H.T.; Padilla, W.J.; Zide, J.M.O.; Gossard, A.C.; Taylor, A.J.; Averitt, R.D. Active terahertz metamaterial devices. *Nature* **2006**, *444*, 597–600. [[CrossRef](#)] [[PubMed](#)]
7. Ju, L.; Geng, B.; Horng, J.; Girit, C.; Martin, M.; Hao, Z.; Bechtel, H.A.; Liang, X.; Zettl, A.; Shen, Y.R.; et al. Graphene plasmonics for tunable terahertz metamaterials. *Nat. Nanotechnol.* **2011**, *6*, 630–634. [[CrossRef](#)]
8. Linden, S.; Enkrich, C.; Wegener, M.; Zhou, J.; Koschny, T.; Soukoulis, C.M. Magnetic response of metamaterials at 100 terahertz. *Science* **2004**, *306*, 1351–1353. [[CrossRef](#)]
9. Bai, J.; Pang, Z.; Shen, P.; Chen, T.; Shen, W.; Wang, S.; Chang, S. A terahertz photo-thermoelectric detector based on metamaterial absorber. *Opt. Commun.* **2021**, *497*, 127184. [[CrossRef](#)]
10. Carranza, I.E.; Grant, J.P.; Gough, J.; Cumming, D. Terahertz metamaterial absorbers implemented in CMOS technology for imaging applications: Scaling to large format focal plane arrays. *IEEE J. Sel. Top. Quantum Electron.* **2016**, *23*, 1–8. [[CrossRef](#)]
11. Che, Z.; Zhang, G.; Ren, P.; Yue, J.; Li, Z.; Lun, Y.; Suo, J.; Zhu, J.; Zhang, Q.; Feng, Y. Narrow bandpass filter based on vanadium dioxide can be used for terahertz stealth. *J. Opt.* **2022**, *51*, 336–342. [[CrossRef](#)]
12. Landy, N.I.; Sajuyigbe, S.; Mock, J.J.; Smith, D.R.; Padilla, W.J. Perfect metamaterial absorber. *Phys. Rev. Lett.* **2008**, *100*, 207402. [[CrossRef](#)]
13. Shen, X.; Yang, Y.; Zang, Y.; Gu, J.; Han, J.; Zhang, W.; Jun Cui, T. Triple-band terahertz metamaterial absorber: Design, experiment, and physical interpretation. *Appl. Phys. Lett.* **2012**, *101*, 154102. [[CrossRef](#)]
14. Zhang, Y.; Feng, Y.; Zhu, B.; Zhao, J.; Jiang, T. Graphene based tunable metamaterial absorber and polarization modulation in terahertz frequency. *Opt. Express* **2014**, *22*, 22743–22752. [[CrossRef](#)] [[PubMed](#)]
15. Huang, L.; Chowdhury, D.R.; Ramani, S.; Reiten, M.T.; Luo, S.N.; Taylor, A.J.; Chen, H.T. Experimental demonstration of terahertz metamaterial absorbers with a broad and flat high absorption band. *Opt. Express* **2012**, *37*, 154–156. [[CrossRef](#)]
16. Agarwal, S.; Srivastava, G.; Prajapati, Y.K. Dual band Vis-IR absorber using bismuth based helical metamaterial surface. *Opt. Quantum Electron.* **2022**, *54*, 772. [[CrossRef](#)]
17. Islam, M.S.; Sultana, J.; Biabanifard, M.; Vafapour, Z.; Nine, M.J.; Dinovitser, A.; Cordeiro, C.M.B.; Ng, B.W.H.; Abbott, D. Tunable localized surface plasmon graphene metasurface for multiband superabsorption and terahertz sensing. *Carbon* **2020**, *158*, 559–567. [[CrossRef](#)]
18. Du, C.; Zhou, D.; Guo, H.H.; Pang, Y.Q.; Shi, H.Y.; Liu, W.F.; Su, J.Z.; Singh, C.; Trukhanov, S.; Trukhanov, A.; et al. An ultra-broadband terahertz metamaterial coherent absorber using multilayer electric ring resonator structures based on anti-reflection coating. *Nanoscale* **2020**, *12*, 9769–9775. [[CrossRef](#)]
19. Liu, Y.; Gu, S.; Luo, C.; Zhao, X. Ultra-thin broadband metamaterial absorber. *Appl. Phys. A* **2012**, *108*, 19–24. [[CrossRef](#)]
20. Agarwal, S.; Prajapati, Y.K. Design of broadband absorber using 2-D materials for thermo-photovoltaic cell application. *Opt. Commun.* **2018**, *413*, 39–43. [[CrossRef](#)]
21. Gu, S.; Barrett, J.P.; Hand, T.H.; Popa, B.I.; Cummer, S.A. A broadband low-reflection metamaterial absorber. *J. Appl. Phys.* **2010**, *108*, 064913. [[CrossRef](#)]
22. Hedayati, M.K.; Javaherirahim, M.; Mozooni, B.; Abdelaziz, R.; Tavassolizadeh, A.; Chakravadhanula, V.S.K.; Zaporozhchenko, V.; Strunkus, T.; Faupel, F.; Elbahri, M. Design of a perfect black absorber at visible frequencies using plasmonic metamaterials. *Adv. Mater.* **2011**, *23*, 5410–5414. [[CrossRef](#)]
23. Yu, P.; Besteiro, L.V.; Huang, Y.; Wu, J.; Fu, L.; Tan, H.H.; Jagadish, C.; Wiederrecht, G.P.; Govorov, A.O.; Wang, Z. Broadband metamaterial absorbers. *Adv. Opt. Mater.* **2019**, *7*, 1800995. [[CrossRef](#)]
24. Xie, T.; Chen, D.; Yang, H.; Xu, Y.; Zhang, Z.; Yang, J. Tunable broadband terahertz waveband absorbers based on fractal technology of graphene metamaterial. *Nanomaterials* **2021**, *11*, 269. [[CrossRef](#)]
25. Naveed, M.A.; Bilal, R.M.H.; Baqir, M.A.; Bashir, M.M.; Ali, M.M.; Rahim, A.A. Ultrawideband fractal metamaterial absorber made of nickel operating in the UV to IR spectrum. *Opt. Express* **2021**, *29*, 42911–42923. [[CrossRef](#)]
26. Bilal, R.M.H.; Naveed, M.A.; Baqir, M.A.; Ali, M.M.; Rahim, A.A. Design of a wideband terahertz metamaterial absorber based on Pythagorean-tree fractal geometry. *Opt. Mater. Express* **2020**, *10*, 3007–3020. [[CrossRef](#)]
27. Gottheim, S.; Zhang, H.; Govorov, A.O.; Halas, N.J. Fractal nanoparticle plasmonics: The Cayley tree. *ACS Nano* **2015**, *9*, 3284–3292. [[CrossRef](#)]
28. Zubair, A.; Zubair, M.; Danner, A.; Mehmood, M.Q. Engineering multimodal spectrum of Cayley tree fractal meta-resonator supercells for ultrabroadband terahertz light absorption. *Nanophotonics* **2020**, *9*, 633–644. [[CrossRef](#)]
29. Agarwal, S.; Prajapati, Y.K. Analysis of metamaterial-based absorber for thermo-photovoltaic cell applications. *IET Optoelectron.* **2017**, *11*, 208–212. [[CrossRef](#)]
30. Huang, J.; Li, J.; Yang, Y.; Li, J.; Li, J.; Zhang, Y.; Yao, J. Broadband terahertz absorber with a flexible, reconfigurable performance based on hybrid-patterned vanadium dioxide metasurfaces. *Opt. Express* **2020**, *28*, 17832–17840. [[CrossRef](#)]
31. Dao, R.N.; Kong, X.R.; Zhang, H.F.; Su, X.R. A tunable broadband terahertz metamaterial absorber based on the vanadium dioxide. *Optik* **2019**, *180*, 619–625. [[CrossRef](#)]

32. Zhou, R.; Jiang, T.; Peng, Z.; Li, Z.; Zhang, M.; Wang, S.; Li, L.; Liang, H.; Ruan, S.; Su, H. Tunable broadband terahertz absorber based on graphene metamaterials and VO<sub>2</sub>. *Opt. Mater.* **2021**, *114*, 110915. [[CrossRef](#)]
33. Agarwal, S.; Prajapati, Y.K. Broadband and polarization-insensitive helix metamaterial absorber using graphene for terahertz region. *Appl. Phys. A* **2016**, *122*, 561. [[CrossRef](#)]
34. Badri, S.H.; Gilarlue, M.M.; SaeidNahaei, S.; Kim, J.S. Narrowband-to-broadband switchable and polarization-insensitive terahertz metasurface absorber enabled by phase-change material. *J. Opt.* **2022**, *24*, 025101. [[CrossRef](#)]
35. Badri, S.H.; Soofi, H.; SaeidNahaei, S. Thermally reconfigurable extraordinary terahertz transmission using vanadium dioxide. *JOSA B* **2022**, *39*, 1614–1621. [[CrossRef](#)]
36. Zhong, Y.; Huang, Y.; Zhong, S.; Lin, T.; Luo, M.; Shen, Y.; Ding, J. Tunable terahertz broadband absorber based on MoS<sub>2</sub> ring-cross array structure. *Opt. Mater.* **2021**, *114*, 110996. [[CrossRef](#)]
37. Liu, L.; Liu, W.; Song, Z. Ultra-broadband terahertz absorber based on a multilayer graphene metamaterial. *J. Appl. Phys.* **2020**, *128*, 093104. [[CrossRef](#)]
38. Wu, T.; Shao, Y.; Ma, S.; Wang, G.; Gao, Y. Broadband terahertz absorber with tunable frequency and bandwidth by using Dirac semimetal and strontium titanate. *Opt. Express* **2021**, *29*, 7713–7723. [[CrossRef](#)] [[PubMed](#)]
39. Liu, Y.; Huang, R.; Ouyang, Z. Numerical Investigation of Graphene and STO Based Tunable Terahertz Absorber with Switchable Bifunctionality of Broadband and Narrowband Absorption. *Nanomaterials* **2021**, *11*, 2044. [[CrossRef](#)]
40. Song, Z.; Chen, A.; Zhang, J. Terahertz switching between broadband absorption and narrowband absorption. *Opt. Express* **2020**, *28*, 2037–2044. [[CrossRef](#)] [[PubMed](#)]
41. Liu, W.; Song, Z. Terahertz absorption modulator with largely tunable bandwidth and intensity. *Carbon* **2021**, *174*, 617–624. [[CrossRef](#)]
42. Otsuka, K.; Ren, X. Physical metallurgy of Ti–Ni-based shape memory alloys. *Prog. Mater. Sci.* **2005**, *50*, 511–678. [[CrossRef](#)]
43. Cao, J.; Zhou, J.; Li, M.; Chen, J.; Zhang, Y.; Liu, X. Insightful understanding of three-phase interface behaviors in 1T-2H MoS<sub>2</sub>/CFP electrode for hydrogen evolution improvement. *Chin. Chem. Lett.* **2022**, *33*, 3745–3751. [[CrossRef](#)]
44. Tan, C.; Liu, J.; Tian, X.; Zhu, J.; Zhang, K. Multifunctional and dynamically tunable terahertz metamaterials based on TiNi shape memory alloy films with a simple design. *Results Phys.* **2021**, *24*, 104165. [[CrossRef](#)]
45. Zhang, K.; Ma, T.; Liu, J.; Tian, X.; Zhu, J.; Tan, C. Dynamically tunable and polarization-insensitive dual-band terahertz metamaterial absorber based on TiNi shape memory alloy films. *Results Phys.* **2021**, *23*, 104001. [[CrossRef](#)]
46. Kainuma, R.; Imano, Y.; Ito, W.; Sutou, Y.; Morito, H.; Okamoto, S.; Kitakami, O.; Oikawa, K.; Fujita, A.; Kanomata, T.; et al. Magnetic-field-induced shape recovery by reverse phase transformation. *Nature* **2006**, *439*, 957–960. [[CrossRef](#)] [[PubMed](#)]
47. Thomas, M.; Heczko, O.; Buschbeck, J.; Lai, Y.W.; McCord, J.; Kaufmann, S.; Schultz, L.; Fähler, S. Stray-Field-Induced Actuation of Free-Standing Magnetic Shape-Memory Films. *Adv. Mater.* **2009**, *21*, 3708–3711. [[CrossRef](#)]
48. Zhang, K.; Tan, C.; Zhao, W.; Guo, E.; Tian, X. Computation-Guided Design of Ni–Mn–Sn Ferromagnetic Shape Memory Alloy with Giant Magnetocaloric Effect and Excellent Mechanical Properties and High Working Temperature via Multielement Doping. *ACS Appl. Mater. Interfaces* **2019**, *11*, 34827–34840. [[CrossRef](#)]
49. Wang, X.; Liu, X.; Zhang, K.; Liu, R.; Zhu, J.; Tian, X.; Tan, C. Magnetic-induced dual-function tunable THz polarization conversion metamaterial based on Ni–Mn–Sn shape memory alloy films. *Results Opt.* **2022**, *9*, 100274. [[CrossRef](#)]
50. Zheng, C.; Li, J.; Wang, S.; Li, J.; Li, M.; Zhao, H.; Hao, X.; Zang, H.; Zhang, Y.; Yao, J. Optically tunable all-silicon chiral metasurface in terahertz band. *Appl. Phys. Lett.* **2021**, *118*, 051101. [[CrossRef](#)]
51. Shabanpour, J. Programmable anisotropic digital metasurface for independent manipulation of dual-polarized THz waves based on a voltage-controlled phase transition of VO<sub>2</sub> microwires. *J. Mater. Chem. C* **2020**, *8*, 7189–7199. [[CrossRef](#)]
52. Pan, W.; Yan, Y.; Ma, Y.; Shen, D. A terahertz metamaterial based on electromagnetically induced transparency effect and its sensing performance. *Opt. Commun.* **2019**, *431*, 115–119. [[CrossRef](#)]
53. Bisht, S.; Saini, S.; Prakash, V.; Nautiyal, B. Study the various feeding techniques of microstrip antenna using design and simulation using CST microwave studio. *Int. J. Emerg. Technol. Adv. Eng.* **2014**, *4*, 318–324.
54. Liu, A.Q.; Zhu, W.M.; Tsai, D.P.; Zheludev, N.I. Micromachined tunable metamaterials: A review. *J. Opt.* **2021**, *14*, 114009. [[CrossRef](#)]
55. Kim, H.; Melinger, J.S.; Khachatryan, A.; Charipar, N.A.; Auyeung, R.C.Y.; Piqué, A. Fabrication of terahertz metamaterials by laser printing. *Opt. Lett.* **2010**, *35*, 4039–4041. [[CrossRef](#)]
56. Walther, M.; Ortner, A.; Meier, H.; Löffelmann, U.; Smith, P.J.; Korvink, J.G. Terahertz metamaterials fabricated by inkjet printing. *Appl. Phys. Lett.* **2009**, *95*, 251107. [[CrossRef](#)]
57. Smith, D.R.; Vier, D.C.; Koschny, T.; Soukoulis, C.M. Electromagnetic parameter retrieval from inhomogeneous metamaterials. *Phys. Rev. E* **2005**, *71*, 036617. [[CrossRef](#)] [[PubMed](#)]
58. Smith, D.R.; Schultz, S.; Markoš, P.; Soukoulis, C.M. Determination of effective permittivity and permeability of metamaterials from reflection and transmission coefficients. *Phys. Rev. B* **2002**, *65*, 195104. [[CrossRef](#)]
59. Auge, A.; Teichert, N.; Meinert, M.; Reiss, G.; Hütten, A.; Yüzüak, E.; Dincer, I.; Elerman, Y.; Ennen, I.; Schattschneider, P. Thickness dependence of the martensitic transformation, magnetism, and magnetoresistance in epitaxial Ni–Mn–Sn ultrathin films. *Phys. Rev. B* **2012**, *85*, 214118. [[CrossRef](#)]
60. Krenke, T.; Acet, M.; Wassermann, E.F.; Moya, X.; Mañosa, L.; Planes, A. Martensitic transitions and the nature of ferromagnetism in the austenitic and martensitic states of Ni–Mn–Sn alloys. *Phys. Rev. B* **2005**, *72*, 014412. [[CrossRef](#)]

61. Rao, Y.; Pan, L.; Ouyang, C.; Xu, Q.; Liu, L.; Li, Y.; Zhang, W. Asymmetric transmission of linearly polarized waves based on Mie resonance in all-dielectric terahertz metamaterials. *Opt. Express* **2020**, *28*, 29855–29864. [[CrossRef](#)]
62. Chen, H.T. Interference theory of metamaterial perfect absorbers. *Opt. Express* **2012**, *20*, 7165–7172. [[CrossRef](#)] [[PubMed](#)]
63. Gu, J.; Singh, R.; Liu, X.; Zhang, X.; Ma, Y.; Zhang, S.; Zhang, W. Active control of electromagnetically induced transparency analogue in terahertz metamaterials. *Nat. Commun.* **2012**, *3*, 1151. [[CrossRef](#)]
64. Li, J.S.; Li, X.J. Switchable tri-function terahertz metasurface based on polarization vanadium dioxide and photosensitive silicon. *Opt. Express* **2022**, *30*, 12823. [[CrossRef](#)] [[PubMed](#)]
65. Bing, P.; Guo, X.; Wang, H.; Li, Z.; Yao, J. Characteristic analysis of a photoexcited tunable metamaterial absorber for terahertz waves. *J. Opt.* **2019**, *48*, 179–183. [[CrossRef](#)]
66. Pitchappa, P.; Kumar, A.; Liang, H.; Prakash, S.; Wang, N.; Bettiol, A.A.; Venkatesan, T.; Lee, C.; Singh, R. Frequency-Agile Temporal Terahertz Metamaterials. *Adv. Opt. Mater.* **2020**, *8*, 2000101. [[CrossRef](#)]
67. Ou, J.Y.; Plum, E.; Zhang, J.; Zheludev, N.I. An electromechanically reconfigurable plasmonic metamaterial operating in the near-infrared. *Nat. Nanotechnol.* **2013**, *8*, 252–255. [[CrossRef](#)]
68. Butera, F. Shape memory actuators for automotive applications. *Adv. Mater. Process.* **2008**, *166*, 37.
69. Jani, J.M.; Leary, M.; Subic, A.; Gibson, M.A. A review of shape memory alloy research, applications and opportunities. *Mater. Des.* **2014**, *56*, 1078–1113. [[CrossRef](#)]
70. Strelec, J.K.; Lagoudas, D.C.; Khan, M.A.; Yen, J. Design and implementation of a shape memory alloy actuated reconfigurable airfoil. *J. Intell. Mater. Syst. Struct.* **2003**, *14*, 257–273. [[CrossRef](#)]
71. Karami, M.; Chen, X. Nanomechanics of shape memory alloys. *Mater. Today Adv.* **2021**, *10*, 100141. [[CrossRef](#)]
72. Gupta, B.; Pandey, S.; Nahata, A.; Zhang, T.; Nahata, A. Bistable physical geometries for terahertz plasmonic structures using shape memory alloys. *Adv. Opt. Mater.* **2017**, *5*, 1601008. [[CrossRef](#)]
73. Zhou, H.; Zhang, T.; Guruswamy, S.; Nahata, A. An electrically tunable terahertz plasmonic device based on shape memory alloys and liquid metals. *Adv. Opt. Mater.* **2018**, *6*, 1700684. [[CrossRef](#)]
74. Valente, J.; Ou, J.Y.; Plum, E.; Youngs, I.J.; Zheludev, N.I. Reconfiguring photonic metamaterials with currents and magnetic fields. *Appl. Phys. Lett.* **2015**, *106*, 111905. [[CrossRef](#)]

**Disclaimer/Publisher’s Note:** The statements, opinions and data contained in all publications are solely those of the individual author(s) and contributor(s) and not of MDPI and/or the editor(s). MDPI and/or the editor(s) disclaim responsibility for any injury to people or property resulting from any ideas, methods, instructions or products referred to in the content.